ELSEVIER

Journal of Power Sources 58 (1996) 109–122

JOURNAL OF POWER SOURCES

Three-dimensional numerical simulation for various geometries of solid oxide fuel cells

J.R. Ferguson [a], J.M. Fiard [b], R. Herbin [c]

[a] *Zentralstrasse 139, 5430 Wettingen, Switzerland*

[b] *Program in Applied Mathematics, UC Boulder, CO 80309-0526, USA*

[c] *Centre de Mathématiques et d'Informatique, Université de Provence, 39 rue F. Joliot-Curie, 13453 Marseille Cedex 13, France*

Received 28 July 1995; revised 15 August 1995; accepted 3 October 1995

Abstract

A three-dimensional mathematical model of a solid oxide fuel cell is presented, which allows the computation of the local distributions of the electrical potential, temperature and concentration of the chemical species. The physics of the cell and the simplifying assumptions are presented; a sketch of the numerical procedure is also given. The numerical results obtained with hydrogen as the fuel are compared with results from other simulation codes which were developed for a planar geometry. The numerical results show the behaviour of the potential, temperature and current distributions when certain parameters (geometry of the cell, electrolyte materials, temperature in the channels) are varied. Numerical simulation is also used to obtain an optimum for some geometry parameters such as cathode thickness or rib width.

Keywords: Solid oxide fuel cells; Numerical simulation; Mathematical modelling

1. Introduction

The work presented here deals with the mathematical modelling and numerical simulation of natural gas-fed solid oxide fuel cells (SOFCs) under a stationary regime. The principle of an SOFC is based on the conversion of the chemical energy, which is stored in the fuel (hydrogen or methane), into electrical energy through an electron-producing electrochemical reaction (see e.g. Ref. [1]). The electrical energy produced by an electrochemical reaction depends on the concentration of the reacting species through the Nernst law. A schematic diagram of the electrochemical processes is given in Fig. 1:

1. oxygen diffuses through the porous cathode material;
2. oxygen molecules are dissociated and ionized at the cathode/electrolyte interface;
3. oxygen ions migrate through the electrolyte towards the anode/electrolyte interface;
4. fuel diffuses through the porous anode material; and
5. hydrogen contained in (and/or produced by) the fuel reacts with oxygen ions, producing water and liberating electrons, that flow back to the cathode/electrolyte interface, via an external circuit.

Hydrogen can be produced from methane, and an interesting feature of an SOFC is the fact that it runs at a temperature which is sufficiently high to allow internal reforming, which is taken into account in the present model. The SOFC systems seem to be of great interest for the use of natural gas, because of their high power generation and heat recovery efficiency, as well as their low pollution rate. Moreover, the electrolyte in an SOFC is solid rather than liquid (as for instance in a phosphoric acid fuel cell) and, therefore, there is no need to handle corrosive liquids. Because of their high temperature operating conditions, internal reforming of methane is possible, along with heat generation from the hot steam which is produced by the cell. However, the ideal efficiency rate is never attained in experimental conditions. Important losses seem to be internal ohmic losses; diffusion losses and over-

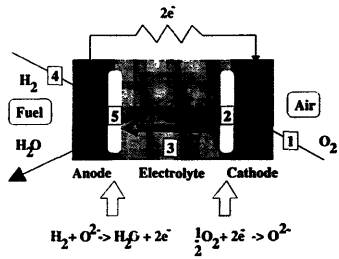

Fig. 1. Electrochemical processes in a SOFC.

SSDI 0378-7753(95)02269-0

potential due to the electrochemical reactions can also be expected. The aim of the mathematical modelling and numerical simulation of such a system is to give, for a given set of data describing the geometry of the cell and the operating conditions, an estimate of these losses and where they occur. Also, by varying the set of input parameters describing either the geometry or the operating conditions, the influence of these parameters on the efficiency of the cell can be studied. Hence modelling may be viewed as a design tool.

Numerical simulation of SOFCs has already been performed with mathematical models which were obtained with some simplifying assumptions (see Refs. [2,3], and references therein). A two-dimensional mathematical model of the cross section of a planar SOFC has also been developed [4,5]; in these works, as in the present work, the temperature, distribution, concentration of the species and electrical current are obtained within the unit cell itself, whereas in other works, which are concerned with the modelling of a whole stack, the solid materials were assumed to be all at the same temperature, and the current density was computed by averaging the conductivities of the various components [6–8]. A number of models of the unit cell also exist which were tested on a benchmark defined in a International Energy Agency (IEA) workshop [9–11]. The originality of the present work lies in the fact that it yields the local distribution of temperature, electric potential and concentration in a three-dimensional unit cell for various geometries; it uses a flux-conservative discretization scheme, the 'finite volume' scheme (see e.g. Refs. [12,13]) to do so.

The following sections are organized as follows: Section 2 is devoted to the description of the unit cell geometry and, more precisely, to the geometries which have already been implemented in the numerical code. Section 3 deals with the mathematical model itself, i.e. the governing equations and the boundary conditions which were defined in order to compute the local distributions. Section 4 describes the numerical procedure and the computer code which uses this procedure. The validation of the code is demonstrated in Section 5 by running it with the data of the benchmark defined in an IEA workshop [9] and comparing it with other numerical codes. In Section 6, we show how the numerical code can be viewed as a design tool. First, the efficiencies of the parallel and cross-flow cases are compared; second, the influence of the electrode thickness on the efficiency of the cell is studied. In the case of internal reforming, an optimum value of the anode thickness can be computed. Finally, numerical results for cylindrical and tubular geometries are shown.

2. Description of the geometry

The SOFC system is in fact a stack of electrochemical cells, i.e. it is made up of several repeating 'unit cells'. The layout of the mathematical equations describing the physical and chemical phenomena can be carried out on the smallest non-repeating geometrical pattern which represents the unit cell. Several concepts exist for SOFCs, based on the geometry and the materials used for the different components of the cell. One of these concepts is the so-called 'planar bi-polar' geometry, see Fig. 2. This concept includes the 'co-flow' and 'counter-flow' cases where the air and gas channels are parallel, and the 'cross-flow' case where the channels are perpendicular. The latter case is preferred by industry because of the simplicity of the manifolding.

The results of Ref. [3], which are based on a one-dimensional model along the channel direction (i.e. a two-dimensional model in the case of a cross-flow configuration) indicate that the co-flow geometry should be the most efficient. This is also the case in the model developed in Ref. [14]. In a previous paper [15], the model of the cross section of parallel flow configuration was developed. This model is generalized here for a three-dimensional unit cell; the geometries which are considered are the planar concept, with co-, counter- or cross-flow designs; our numerical code can also handle the tubular concept developed by Westinghouse, depicted in Fig. 3, and the cylindrical geometry, sketched in

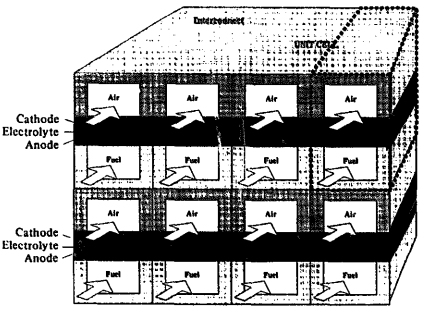

Fig. 2. The planar concept for SOFCs.

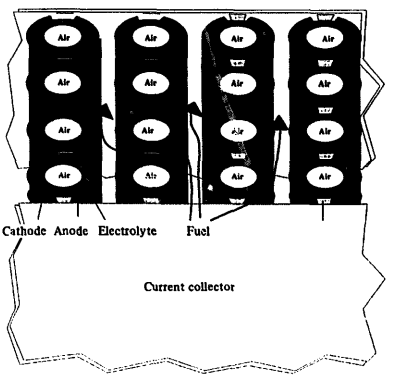

Fig. 3. The tubular concept for SOFCs.

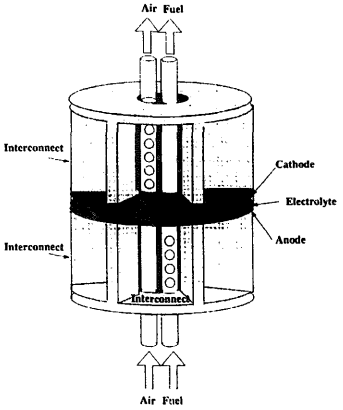

Fig. 4. The cylindrical concept for SOFCs.

Fig. 4. The code is also designed to be able to treat other geometries if necessary. The unit-cell mathematical model is independent of the cell geometry. It has to be formulated before carrying out the numerical computations which will yield the behaviour of the physical entities for one unit cell. It can also be used to compute the same physical entities for a whole stack provided that the stack is made up of the same repeating unit cells, and that the boundary conditions at the channel walls are independent of the cells (i.e. same concentration of species and same temperatures), with adequate boundary conditions on the exterior of the stack (thermal and electrical insulation). So as to leave no doubt, the various parameters on a planar bi-polar co- or counter-flow geometry are given in Fig. 5. The cell is built around a PEN (positive electrode/electrolyte/negative electrode) sandwich, where the electrochemical processes occur. The interconnect material, I, supports the structure and also serves as the current collector; it is assumed to be made of a non-porous material, and the diffusion of oxygen only takes place through the cathode, C. The fuel methane diffuses through the porous anode, A, and is transformed into hydrogen by a series of chemical reactions, known as reforming, in the presence of a catalyst, throughout the anode, A; E is the electrolyte, and Ω_S the solid part of the domain of study (i.e. anode, cathode, electrolyte and interconnect); Ch_f and Ch_a are the fuel and air channels. Note that in a two-dimensional model of a cross section, the temperature and concentration are assumed to be given within Ch_f and Ch_a, and therefore the domain of study is Ω_S only [15]. The respective boundaries of these channels will be denoted by Γ_{Ch_a} and Γ_{Ch_f}.

In the case of the tubular concept, the definition of the interfaces must be somewhat altered to take into account the fact that the electrolyte is insulated from the interconnect; the associated interface conditions are, however, quite easy to implement.

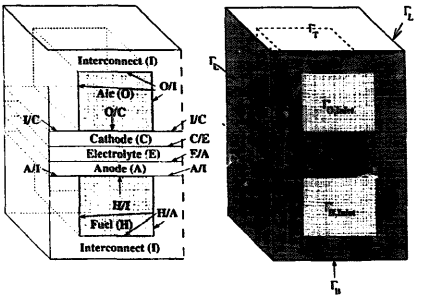

Fig. 5. Geometry of a unit cell.

3. Mathematical model of a unit cell

3.1. Conservation laws

Let Φ denote the electric potential, T the temperature and X_i the molar concentration of species i ($i = O_2, N_2, H_2, H_2O, CO, CO_2, CH_4$). The potential Φ is defined throughout Ω_S, and is continuous everywhere except at the electrode/electrolyte interfaces C/E and E/A; the temperature, T, is defined and continuous throughout Ω_S. The oxygen molar fraction X_{O_2} (and similarly the molar fractions X_i, $i = H_2, H_2O, CO, CO_2, CH_4$) is defined and continuous in the cathode, C (or anode, A). The mathematical model is obtained by writing the conservation laws for the heat flux q, the electric current j, and the mass flux N_i, $i = O_2, N_2, H_2, H_2O, CO, CO_2, CH_4$:

$$\mathrm{div}(j) = 0 \text{ in I, C, E and A} \quad (1)$$

$$\mathrm{div}(q) = Q \text{ in I, C, E, A, } Ch_a \text{ and } Ch_f \quad (2)$$

$$\mathrm{div}(N_i) = 0 \text{ for } i = O_2 \text{ and } N_2 \text{ in C and } Ch_a \quad (3)$$

$$\mathrm{div}(N_i) = r_i$$

$$\text{for } i = H_2, H_2O, CO, CO_2 \text{ and } CH_4 \text{ in A and } Ch_f \quad (4)$$

where $\mathrm{div}\, g = \partial g_1/\partial x + \partial g_2/\partial y + \partial g_3/\partial z$ for any vector-valued function $g = (g_1, g_2, g_3)^T$, x, y, z representing the three space coordinates. Q is the heat source term (arising from the passage of electric current and from the chemical reactions), and r_i the production rate of species i. The fluxes q, j, N_i and the source terms Q and r_i must now be related to the unknowns T, Φ and X_i.

In the above equations, it is assumed that:

1. the electron–chemical reactions occur at the anode/electrolyte and cathode/electrolyte interfaces (i.e. heterogeneous reactions);
2. no chemical reactions occur within the air channel, and
3. reforming and water-shift reactions occur within the fuel channel and anode domains.

3.2. Constitutive laws

In the solid parts, the thermal flux is mainly conductive and modelled by Fourier's law of heat conduction:

$$\boldsymbol{q} = -\lambda \operatorname{grad} T \text{ in I, A, E and C} \tag{5}$$

where grad T denotes the gradient of a scalar function T, i.e. grad $T = (\partial T/\partial x,\ \partial T/\partial y,\ \partial T/\partial z)^{\mathrm{T}}$, and λ is the thermal conductivity.

In the gas channels, the thermal flux is mainly convective in the gas flow direction, and conductive from the channel to the solid parts. Hence the expression for the flux is:

$$\boldsymbol{q} = \sum_{i \in G} C_{pi} N_i T - \lambda \operatorname{grad} T \text{ in } Ch_f \text{ and } Ch_a \tag{6}$$

where G is the set of various components of the gas mixtures, i.e. $G = \{H_2, H_2O, CO, CO_2, CH_4\}$ in Ch_f, whereas $G = \{O_2, N_2\}$ in Ch_a. The electric current is modelled by Ohm's law:

$$\boldsymbol{j} = -\sigma \operatorname{grad} \Phi \text{ in I, A, E and C} \tag{7}$$

where σ is the (temperature-dependent) electric conductivity.

In the porous media (i.e. cathode and anode), the molar fluxes are mainly due to diffusion and satisfy Fick's law of diffusion in a mixture (see e.g. Ref. [16]):

$$N_i = -cD_{i,\mathrm{mix}} \operatorname{grad} X_i + X_i \sum_{j \in G} N_j \text{ in A and C} \tag{8}$$

where c is the concentration and $D_{i,\mathrm{mix}}$ the diffusion coefficient of species i in the considered mixture. In the gas channels, the molar flux is mainly convective in the flow direction and due to molecular diffusion at the boundaries Γ_{Ch_f} and Γ_{Ch_a}, where the mass exchange may be taken into account using a mass-transfer coefficient (see Sections 3.4 and 3.5). Hence the molar flux may be written as:

$$N_i = -cV_k X_i \text{ in } k \text{ (for } k = Ch_a \text{ and } Ch_f)$$

$$\text{for } i = O_2, N_2, H_2, H_2O, CO, CO_2 \text{ and } CH_4 \tag{9}$$

where V_k is the velocity of the mixture in channel k. In fact, we make the additional assumption that the nitrogen flux is zero in the air channel and porous cathode in any channel cross section.

3.3. Source terms

The volumetric heat source term, Q, is in fact the sum of two terms. The first term is the ohmic heat source term and can be written σ grad Φ grad Φ. The second term is the heat produced by the shift and reforming reactions which take place in the porous, catalytic anode, and we shall denote it by Q_{chem}. The shift reaction:

$$CO + H_2O \leftrightarrow CO_2 + H_2 \tag{10}$$

is assumed to be in equilibrium. The heat produced is equal to the term ΔH_S of the reaction; the shift reaction occurs in both the porous anode and the fuel channel. The reforming reaction:

$$CH_4 + H_2O \leftrightarrow 3H_2 + CO \tag{11}$$

is irreversible and thus the heat produced is equal to the enthalpy ΔH_R. Finally, the heat source term can be expressed as:

$$Q = \sigma \operatorname{grad} \Phi \operatorname{grad} \Phi + Q_{\mathrm{chem}} \tag{12}$$

$$Q_{\mathrm{chem}} = \begin{cases} \Delta H_S \text{ in } Ch_f \\ \Delta H_S + \Delta H_R \text{ in A} \\ 0 \text{ elsewhere} \end{cases} \tag{13}$$

The volumetric mass source term r_i is made up of two terms:

$$r_i = \nu^S r^S + \nu^R r^R \tag{14}$$

where r^S and r^R are the volumetric reaction rates of reactions (10) and (11), respectively, and ν^S is the stoichiometric coefficient of reactions (10) and (11). The expression for r^R was taken from the work of Lee [17]:

$$r^R = \rho k_0 \exp(-E^R/RT) P_{CH_4}^{\alpha} P_{H_2O}^{\beta} \tag{15}$$

where ρ is the resistivity of the anode, k_0 the frequency factor, E^R the activation energy of the reforming reaction and α and β the reaction orders of CH_4 and H_2O. The expression and the data given by Lee [17] are used even though the conditions within the fuel cell anode and fuel channel are different from the test conditions. The H_2O partial pressure level and electric field which are present in the SOFC situation [6] may alter the reforming rate. Few data are available within the open literature.

The volumetric reaction rate r^S is computed by assuming the shift reaction to be at equilibrium:

$$K = \frac{X_{CO_2} X_{H_2}}{X_{CO} X_{H_2O}} \tag{16}$$

The conversation laws, Eqs.(1)–(4), the constitutive laws, Eqs. (5)–(9) and the source term expression, Eqs. (12)–(14) yield the following system of (coupled) elliptic equations:

$$\operatorname{div}(-\sigma \operatorname{grad} \Phi) = 0 \text{ in I, C, E and A} \tag{17}$$

$$\operatorname{div}(-\lambda \operatorname{grad} T) = \sigma \operatorname{grad} \Phi \operatorname{grad} \Phi + Q_{\mathrm{chem}} \text{ in I, C, E and A} \tag{18}$$

$$\operatorname{div}\Big(\sum_{i \in G} C_{pi} N_i T - \lambda \operatorname{grad} T\Big) = Q_{\mathrm{chem}} \text{ in } Ch_f \text{ and } Ch_a \tag{19}$$

$$\operatorname{div}\left(-cD_{O_2,\mathrm{mix}} \frac{\operatorname{grad} X_{O_2}}{1 - X_{O_2}}\right) = 0 \text{ in C} \tag{20}$$

$$\operatorname{div}(-cV_{Ch_a} X_i) = 0 \text{ for } i = O_2 \text{ and } N_2 \text{ in } CH_a \tag{21}$$

$$\operatorname{div}\Big(-cD_{i,\mathrm{mix}} \operatorname{grad} X_i + X_i \sum_{j \in G} N_j\Big) = r_i$$

$$\text{for } i = H_2, H_2O, CO, CO_2 \text{ and } CH_4 \text{ in A} \tag{22}$$

$$\operatorname{div}(-cV_{Ch_f} X_i) = r_i$$

$$\text{for } i = H_2, H_2O, CO, CO_2 \text{ and } CH_4 \text{ in } Ch_f \tag{23}$$

3.4. Interface conditions

Due to the surface electrochemical reactions, discontinuities of the potential and heat flux at the electrode/electrolyte interfaces exist. Also, in the three-dimensional model, the heat and mass transfer between the gas channel and the solid parts will be taken into account as interface conditions. Note that in the two-dimensional model these become boundary conditions, since the temperature and the concentration in the channels are then data to the model.

The interface conditions on the various unknowns and associated fluxes are given in the following sections.

3.4.1. Temperature and heat flux

The temperature is continuous throughout the solid domain. We shall model the boundary layer which exists external to the channel walls by a heat-transfer law of the form:

$$[q\cdot n]_S = h(T_S - T_G) \tag{24}$$

where $[q\cdot n]_S$ is the outward normal flux to the solid wall, h the heat-transfer coefficient, T_S is the temperature of the solid wall and T_G the temperature of the gas.

The heat flux is continuous everywhere except at the anode/electrolyte interface, where the electrochemical reaction generates a heat source term:

$$[q\cdot n]_E + [q\cdot n]_A = \frac{[j\cdot n]_A}{2F} T\,\Delta S \text{ at E/A} \tag{25}$$

where ΔS is the entropy of the reaction

$$0.5O_2 + H_2 \leftrightarrow H_2O \tag{26}$$

Note that this model does not take into account the effect of radiation. Work is under progress to include the radiation equations in the unit cell model [18]; these generate a 4th-order nonlinearity which requires a specific numerical procedure.

3.4.2. Species concentration and mass flux

The species concentrations, X_i, are studied in the channels and the porous electrodes. The conservation of the electrons must be written at the interfaces where the electrochemical reactions occur. Hence the mass flux is related to the electric current by Faraday's law:

$$[N_{O_2}\cdot n]_C = \frac{[j\cdot n]_E}{4F} \text{ at C/E} \tag{27}$$

$$[N_{H_2}\cdot n]_A = \frac{[j\cdot n]_A}{2F} \text{ at E/A} \tag{28}$$

3.4.3. Potential and electric currents

The potential is continuous throughout the solid parts except at the electrode/electrolyte interfaces where the electrochemical reactions occur. These potential jumps are modelled by Nernst's law and are as follows:

$$\Phi_C - \Phi_E = \frac{RT}{4F}\ln(X_{O_2}) - R_{O_2}[j\cdot n]_E \tag{29}$$

$$\Phi_E - \Phi_A = -\frac{\Delta G}{2F} - \frac{RT}{2F}\ln\left(\frac{X_{H_2O}}{X_{H_2}}\right) - R_{H_2}[j\cdot n]_A \tag{30}$$

where ΔG is the Gibbs free energy change of reaction (26), and R_{O_2} and R_{H_2} are the polarization resistivities.

The electric current is continuous everywhere in the solid part, and is linked to the mass flux at the electrode/electrolyte interfaces by Faraday's law, Eqs. (27) and (28).

At the channel/solid interface, the electric current is of course zero, hence the condition:

$$\sigma\ \text{grad}\ \Phi\cdot n = 0 \text{ on } \Gamma_{Ch_a} \text{ and } \Gamma_{Ch_f} \tag{31}$$

3.5. External boundary conditions

The boundary conditions on Φ, T and X_i (and/or on the associated fluxes) on the external boundary of the cell remain to be stated. These boundary conditions depend on the operating conditions (see Fig. 6). The boundary conditions considered here are based on the idea that the cell is part of a whole stack and that the overall behaviour is periodic. Therefore, on the lateral boundary Γ_L we state that:

$$[j\cdot n]_{\Gamma_L} = 0 \tag{32}$$

$$[q\cdot n]_{\Gamma_L} = 0 \tag{33}$$

$$[N_i\cdot n]_{\Gamma_L} = 0 \tag{34}$$

for $i = O_2$, H_2, H_2O, CO, CO_2 and CH_4.

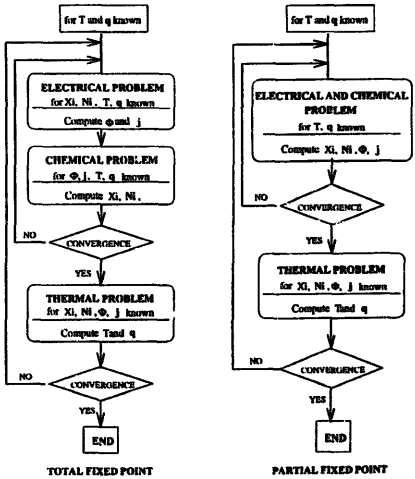

Fig. 6. Solution procedure.

Periodicity conditions are imposed for the temperature on the top and bottom of the cell, whereas a mean current value j_{avg} is imposed for the current, i.e.:

$$[T]_{\Gamma_T} = [T]_{\Gamma_B} \quad (35)$$

$$[q \cdot n]_{\Gamma_T} = -[q \cdot n]_{\Gamma_B} \quad (36)$$

$$[j \cdot n]_{\Gamma_T} = [j \cdot n]_{\Gamma_B} \quad (37)$$

$$[j \cdot n]_{\Gamma_T} = j_{avg} \quad (38)$$

Finally the temperature, the molar fractions and the molar flux are imposed at the inlet face of the gas channels.

4. Numerical implementation

4.1. Numerical procedure

The necessary step in order to perform a numerical simulation is to discretize the set of equations in T, Φ and X_i. The equations themselves are of the Laplace type in the solid part and can be successfully discretized by any of the usual methods, i.e. finite differences, finite elements or finite volumes. However, a finite volume discretization (see Refs. [12,13] for an introduction) was preferred over the finite element method because it is computationally cheaper for the problem at hand, as can be seen from the results shown in Ref. [15]. Moreover, an advantage of the finite volume method is that it is 'close to the physics' in the sense that it is based on writing the balance of the fluxes through the boundaries of a discretization cell (which is called a 'control volume'), and therefore all source terms can be accounted for in a natural way. The discretization of the equations yields a nonlinear finite system, where the unknown parameters are the average values (over the control volumes) of T, Φ and X_i.

The equations in T, Φ, X_i are coupled by the electric conductivity (which depends on the temperature), the ohmic source terms and the interface source terms, both in T and Φ. A rather straightforward iterative method is used, which computes, for a given temperature, the solution to the mass and electric problems (X_i and Φ), and once convergence is obtained, solves the temperature problem.

4.2. Computer code

The computer program, called SOFC3D, consists of two parts. The first part is the computational kernel and database manager. It was written using the C language and contains 11 000 instructions. It has been used on several UNIX systems, e.g. Silicon Graphics, SUN and CRAY. The database input file contains the parameters which define the geometries (planar, cylindrical or tubular), the composition of the fuel (hydrogen or methane), the computational mesh and the set of operating conditions. (Currently, a user-friendly graphic X interface is being developed [19].) The second part is a 10 000 line graphic software which includes a user-friendly mesh generator and a three-dimensional graphics post-processor.

The results which are presented here were obtained on an INDIGO SG workstation with a 50 MHz R4000 processor and 32 MB of real memory. The database file requires about 100 MB of disk memory.

4.3. Validation of the numerical code

Since we have no experimental data to compare with, we validate our code by comparing the results obtained for a benchmark which was defined by participants of the IEA program for the numerical simulation of a planar geometry with 18 fuel and air channels. Note that, throughout these tests, in accordance with the IEA benchmark, the porosity is not taken into account and the thermal conductivity is constant and equal to 2 W m^{-1} K^{-1}. Here, as in Ref. [9], the overpotential at each interface is set to the ohmic loss of the electrolyte. Results are given in Table 1 (results from IEA were taken from Ref. [9]). It appears that in most of the models cited in Table 1, the diffusion effect of the gaseous species in the electrodes is only accounted for in the direction

Table 1
Comparison with the IEA benchmark

Author	Cell voltage		Max. solid temperature		Min. solid temperature	
	Counter-flow	Co-flow	Counter-flow	Co-flow	Counter	Co
Dornier (D)	0.689	0.684	1085	1070	914	928
ECN Petten (NL)		0.704		1082		899
Enericerche (I)	0.730	0.722	1083	1069	906	916
Inst. for Energiteknikk (N)	0.71	0.71	1084	1058	912	930
KFA-Jülich (D)	0.712	0.706	1073	1059	906	913
Siemens (D)	0.716	0.712	1062	1049	904	909
Statoil (N)	0.709	0.702	1082	1098	913	970
Risø (DK)	0.7101	0.7034	1075	1061	910	924
SOFC3D ('3D diff')	0.7080	0.6955	1055	1037	920	921
SOFC3D ('1D diff')	0.7203	0.7079	1054	1036	920	918

Table 2
Gas temperature and composition at inlet

Gas	Temperature (K)	O_2 (%)	N_2 (%)	H_2 (%)	H_2O (%)	CO (%)	CO_2 (%)	CH_4 (%)
Air	1173	21	79					
Fuel I	1173			90	10			
Fuel II	1173			26.26	49.34	2.94	4.36	17.10

orthogonal to the channel axis. We implemented both this 'one-dimensional diffusion' and the three-dimensional diffusion effect. Hence, two series of results from our code are listed in Table 1, labelled '1D diff' and '3D diff'. The '3D diff' cell voltage computed with our code is somewhat smaller than the average cell voltage. However, the '1D diff' cell voltage which we compute is closer to the voltage obtained by the other models. We show in Section 5 that when the three-dimensional effect is accounted for, the concentration profile at the electrode/electrolyte interface is not constant and that the low values of concentrations underneath the rib decreases the efficiency of the cell. The effect of the decrease in activity underneath the rib is recognized to be also of importance in stack modelling [20], it is therefore worth while trying to measure it quantitatively at the cell level.

The code can simulate a cell using pure hydrogen only, or using methane with internal reforming. Tables 2 and 3 give the general operating parameters for both cases, see Ref. [21]. These parameters will be used throughout the numerical runs, unless otherwise mentioned. The following section is devoted to the numerical results which are obtained by running the code on different geometries of adiabatic cells, and the use of these results for cell optimization.

5. Using the code as a design tool

5.1. Comparison of the co-, counter- and cross-flow cases

Numerical tests were performed in the case of the co- and counter-flow for a planar geometry of a 10 cm long unit cell with the following parameters: active area 5.42 mm × 100 mm, anode thickness 50 μm, cathode thickness 50 μm, electrolyte thickness 150 μm, channel width 3 mm, channel height 1 mm, rib width 2.42 mm, and total bipolar plate thickness 2.5 mm.

Fig. 7 gives a comparison of the efficiency, i.e. the ratio of electrical energy to chemical energy at inlet, of a geometry with 5 fuel and air channels for the co-, counter- and cross-flow designs, as a function of current density. In this numerical test, the porosity is not taken into account and the thermal conductivity is constant and equal to 2 $W\,m^{-1}\,K^{-1}$ as in the IEA experiments. The overpotential used is defined in Ref. [9].

These computations show the counter-flow design as being the most efficient. Note that this is in agreement with the results given by the different models of the IEA (see Table 1) but it contradicts the results of Ref. [3], where only the one-dimensional effects were taken into account. The superiority of the counter-flow geometry was also found by numerical experiments on a three-dimensional stack [7] including the reforming effect. This better performance can be explained by the fact that the temperature distribution is better for the efficiency of the reforming reaction.

5.2. Influence of rib width on overall efficiency

The conducting material between two channels is generally called the rib. The rib width seems to be an important parameter for the efficiency of the cell:

1. On one hand, the wider the rib, the smoother is the electrical current. Hence a wider rib will give a better conduction of the electrical current and less ohmic losses.
2. On the other hand, the wider the rib, the narrower is the channel; when the channel width decreases, the chemical species do not diffuse as well underneath the rib.

Therefore, the numerical code can be used to check if an optimal value can be obtained for the rib width. The numerical results confirm the competing effects: when the rib width increases (with all other parameters fixed), the ohmic loss decreases (Fig. 8), but the potential jump also decreases (Fig. 9). With all other parameters set to the values indicated in Tables 2 and 3, an optimal rib width of 2.2 mm is obtained, as indicated in Fig. 10.

5.3. Influence of electrode thickness on efficiency

We study here the influence of the electrode thickness on the concentration of H_2 at the anode/electrolyte interface and on the concentration of O_2 at the cathode/electrolyte interface. It is clear that a thicker interface electrode will be more resistant to the diffusion of the gaseous species; in order to study the significance of this effect we use the two-dimensional pure hydrogen model for a co-flow geometry. We found that the cell voltage which we obtained with our initial model (labelled '3D diff') could be significantly increased if the diffusion of the gas in the porous medium was taken to be only in the direction normal to the electrolyte/anode interface (which is the case in most models and in our simplified model labelled '1D diff'). In our model, however, the diffusion effect is accounted for in all directions, and the hydrogen concentration at the electrode/electrolyte interface is much lower away from the channel than close to it. This is clearly seen in Fig. 11, which represents the hydrogen con-

Table 3
General operating conditions

Average current density	300 mA cm^{-2}
Fuel utilization	85%
Air ratio	7
Pressure	1 bar
Overpotential	see Ref. [8]

Electrical σ ($\Omega^{-1}\,m^{-1}$) and thermal λ ($W\,m^{-1}\,K^{-1}$) conductivities

	Cathode	Electrolyte	Anode	Interconnect
σ	$\frac{4.2\times10^{7}}{T}\exp\left(-\frac{1200}{T}\right)$	$3.34\times10^{4}\exp\left(-\frac{10300}{T}\right)$	$\frac{9.5\times10^{7}}{T}\exp\left(-\frac{1150}{T}\right)$	$\frac{9.3\times10^{5}}{T}\exp\left(-\frac{1100}{T}\right)$
λ	50%		50%	
λ	3	2	3	3.5

Diffusion coefficient	D_{O_2}	D_{H_2}	D_i (Fuel II)
Values ($cm^2\,s^{-1}$)	$0.181\times\left(\frac{T}{273}\right)^{1.5}$	$0.753\times\left(\frac{T}{273}\right)^{1.5}$	$0.364\times\left(\frac{T}{273}\right)^{1.5}$

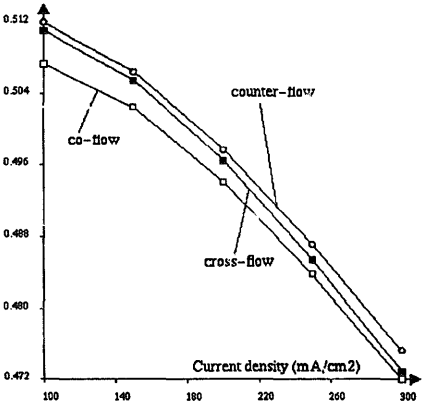

Fig. 7. Efficiency of co-, counter- and cross-flow geometries.

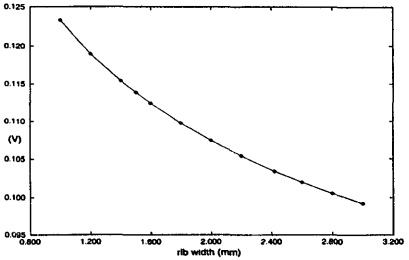

Fig. 8. Ohmic loss vs. rib width.

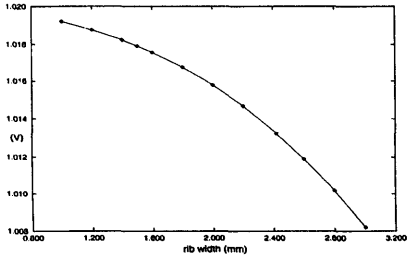

Fig. 9. PEN potential jump vs. rib width.

centration profile for various anode thicknesses, using pure hydrogen as a fuel.

Fig. 12 represents the PEN potential jump computed with the Nernst law with respect to the molar fractions in the channels, at the electrode/electrolyte interface, and with the maximum value of the molar fraction at the electrode/electrolyte interface. Taking this last value is in fact assuming a one-dimensional diffusion in the porous electrode. It is clear from Fig. 12 that the three-dimensional effect in the diffusion loss is quite important, and that it can in fact become dramatic in the case of a narrow anode.

In the case where methane is used, the above results will be altered since the methane reforming rate increases with the anode thickness (and the amount of catalyst), assuming a volumetric reforming reaction. There are now several competing effects which play a role in the optimization of the anode thickness:

1. The diffusion of gas is better for a relatively thin anode (but not too thin, as observed in Fig. 12).

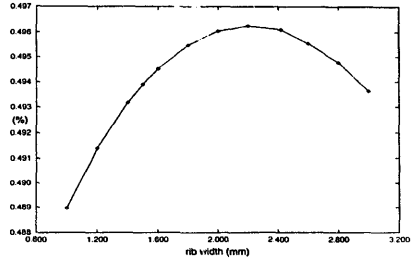

Fig. 10. Efficiency vs. rib width for the pure H_2 model.

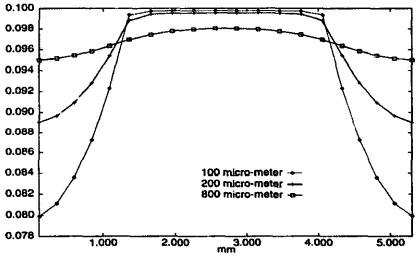

Fig. 11. H_2 molar fraction profile for anode thicknesses of 100, 200 and 800 μm.

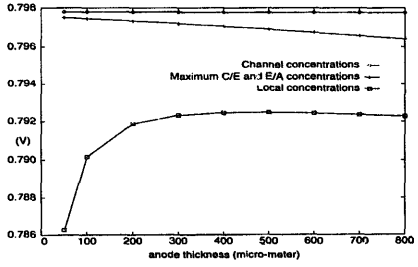

Fig. 12. PEN potential jump vs. anode thickness.

2. The production of methane by volumetric reforming increases with the thickness of the anode (see Fig. 13).
3. The methane reforming is an endothermic reaction, so that when the methane production increases, it decreases the temperature.
4. The ohmic loss increases with the anode thickness, which tends to increase the temperature.

The numerical code simulating the three-dimensional model for methane in the planar geometry was used to study this phenomenon. The input parameters were set as in Tables 2 and 3, with a fixed inlet fuel flux (0.0385 mol/h). The thickness of the anode was varied from 50 to 800 μm. In fact for an anode thickness of 50 μm, there is not sufficient hydrogen produced by reforming for the requested produced current, and the numerical code cannot reach a solution.

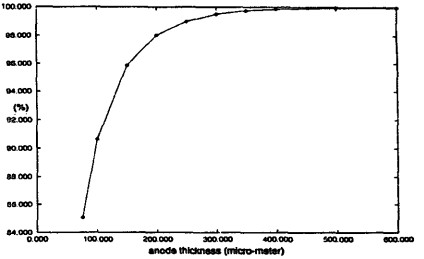

Fig. 13. Methane conversion vs. anode thickness.

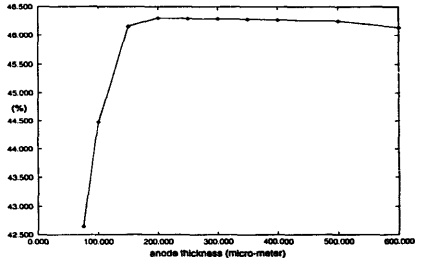

Fig. 14. Efficiency vs. anode thickness.

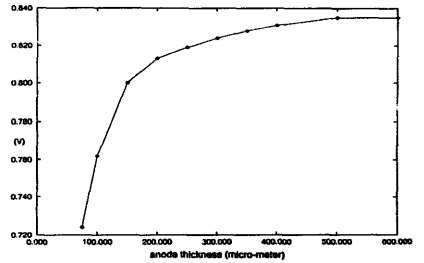

Fig. 15. Nernst potential at the electrolyte level vs. anode thickness.

The results (Fig. 14) show that, for a planar geometry, a thickness of 200 μm seems to be optimal with respect to the efficiency (defined as the ratio of the electric power over the chemical power of the inlet gas). It can be observed from Fig. 15 that the Nernst potential increases steadily with the anode thickness, but so do the ohmic losses (Fig. 16) and the polarization losses (Fig. 17). Note that the fuel utilization decreases with the anode thickness (Fig. 18).

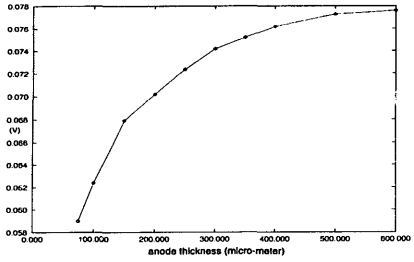

Fig. 16. Ohmic losses vs anode thickness.

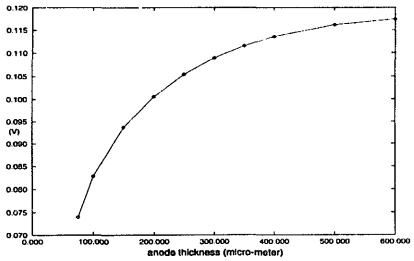

Fig. 17. Polarization losses vs. anode thickness.

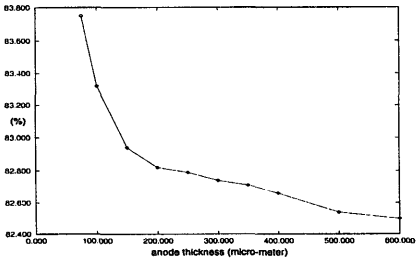

Fig. 18. Fuel utilization.

The minimal temperature may go below the inlet temperature of the fuel because of the endothermic characteristic of the reforming reaction, as may be seen in Fig. 19. This is in agreement with the remarks on a 'cold cell' of Ref. [22]. The rib effect may again be seen in Figs. 20–22.

5.4. Results for other geometries

The adaptivity of our three-dimensional SOFC code can be demonstrated by running numerical simulations on other fundamental geometries. A sample of results concerning a tubular (Westinghouse concept) geometry and a cylindrical geometry are given.

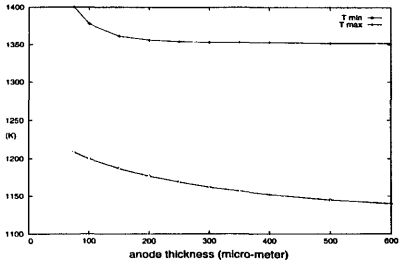

Fig. 19. Maximum and minimum temperatures vs. anode thickness.

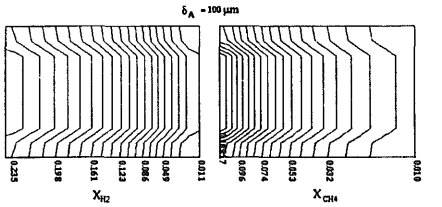

Fig. 20. H_2 and CH_4 molar fractions on a section parallel to the gas channel.

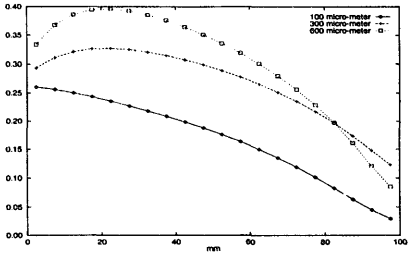

Fig. 21. H_2 molar fraction at the centre point of the anode cross section for several anode thicknesses: 100, 300 and 600 μm.

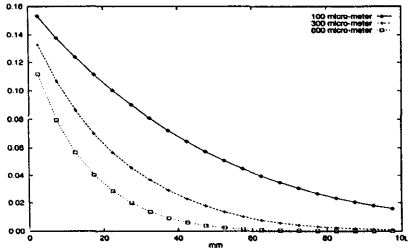

Fig. 22. CH_4 molar fraction at the centre point of the anode cross section for several anode thicknesses: 100, 300 and 600 μm.

5.5. Tubular geometry

In this test, the mean current density is taken equal to 1500 mA cm^{-2} in the interconnect. The dimensions of the cell were taken from Refs. [23,24] and are shown in Fig. 23. This figure also shows the contours of current density at the outlet section of the cell. It can be noted that the highest density is near the interconnect/anode interface; this is due to the fact that the anode is thin, and that the interconnect area is not very large. On the cathode side, however, the current density is lower because the cathode is thicker. Fig. 23 shows the contours of the molar fraction of oxygen and the temperature at the outlet section of the cells. Note that the minimum of the molar fraction of O_2 and the maximum temperature are reached in the region of highest current density (see Fig. 24). Fig. 25 shows the comparison of the potential drops for a planar geometry and a tubular geometry which were chosen such that the input electric current is the same on the upper

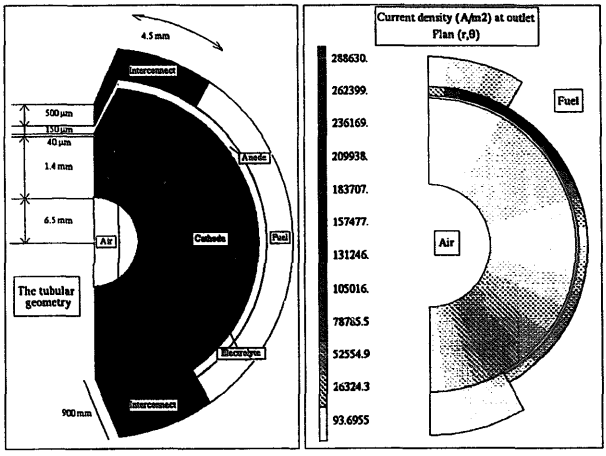

Fig. 23. Three-dimensional section of the tubular design and current density at the outlet section.

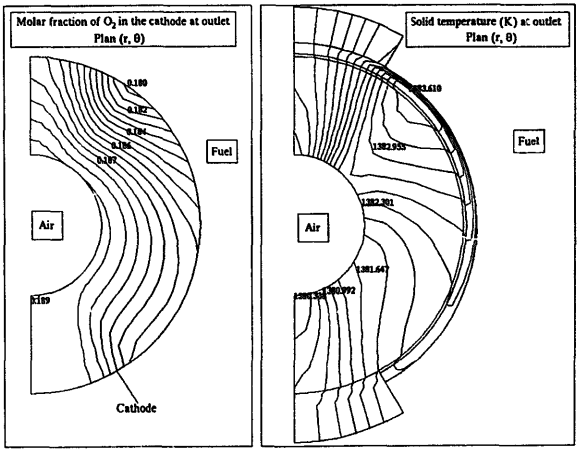

Fig. 24. Molar fraction of O_2 and temperature at the outlet section.

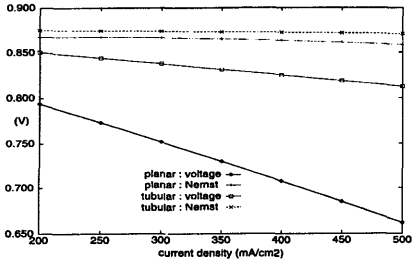

Fig. 25. Comparison of the tubular and planar geometries.

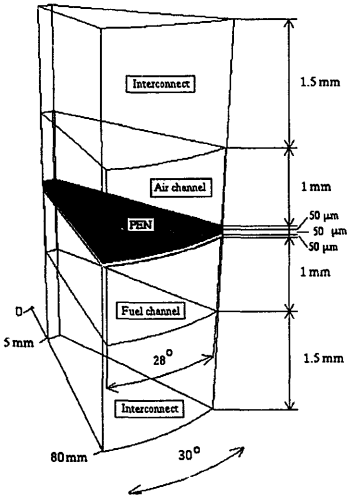

Fig. 26. Geometry of a cylindrical cell.

surface of both geometries. These results show that the tubular geometry is more efficient.

5.6. *Cylindrical geometry*

In the absence of data for a so-called 'cylindrical' geometry, we derived the dimensions of a cylindrical cell by distorting a planar cell. The dimensions of the cell are shown in Fig. 26. The computations were performed on a 'slice' of the cell only, taking symmetry considerations into account. The mean current density is taken equal to 180 mA cm^{-2}. Fig. 27 shows the distribution of temperature in the electrolyte and Fig. 28 the distribution of hydrogen in the anode. Again, one

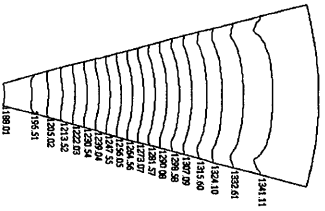

Fig. 27. Temperature distribution in the electrolyte.

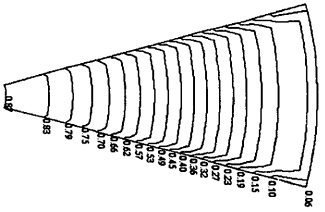

Fig. 28. Molar fractions in the anode.

can see that the diffusion is always weaker at the centre of the rib.

6. Conclusions

A three-dimensional numerical code was developed for the numerical simulation of SOFCs and stacks, which can be used for various geometries of SOFCs. The mathematical model is based on a local balance approach, and the finite volume method was found to be well adapted for our problem. Numerical runs were performed first to validate our code with a benchmark which was defined by the participants of an IEA workshop; the results which were obtained with our code were in good agreement with those of the IEA workshop for the test case (with hydrogen as a fuel), except for the fact that our code seemed to be a little more pessimistic than most others with respect to the electrical potential of the cell. This is probably due to the diffusion effect which our model takes into account more accurately. The code was then used as a design tool for the cell geometry: we compared the cross-, counter- and co-flow designs for a planar geometry and found that the counter-flow was optimal (with hydrogen as a fuel). We also found that we could use the code to compute the optimal value of one given parameter, such as the rib width, or the anode thickness. In the latter case, the reforming effect was studied (using methane as a fuel). Comparisons between the tubular and the planar geometry were carried out, and showed less ohmic loss for the first geometry. The flexibility

of our code allows the simulation of several geometries. Indeed, a new geometry could be introduced relatively easily thanks to the modularity of the code.

Further work includes the study of the effect of the radiation inside the fuel and air channels. In Ref. [22], the effect of radiation was introduced at the stack level by means of the computation of an 'effective thermal conductivity' [22], and it was shown in Ref. [25], using a finite element approach for temperature and electrical current, that the radiation effect has a definite influence on the temperature distribution. A sensitivity analysis with respect to the geometry parameters, the physical properties of the constitutive materials and the operating conditions is also planned.

7. List of symbols

A	anode
c	concentration, mol m^{-3}
C	cathode
Ch_a	air channel
Ch_f	fuel channel
C_{pi}	heat capacity of gas i, kJ $kmol^{-1}$ K^{-1}
$D_{i,mix}$	diffusion coefficient of species i in mixture
E	electrolyte
E	activation energy, kJ kg^{-1} K^{-1}
F	Faraday constant, A s mol^{-1}
h	heat transfer coefficient, W m^{-2} K^{-1}
j	electric current, mA cm^{-2}
K	equilibrium constant
N_i	molar flux for species i, mol s^{-1}
q	heat flux, W s^{-1}
T	temperature, K
Q	heat source term, W m^{-3}
Q_{chem}	heat source term due to chemical reaction, W m^{-3}
V	velocity of gas in channels, m s^{-1}
X_i	molar concentration of species i

Greek symbols

ΔH	enthalpy, kJ
ΔS	entropy, kJ K^{-1}
Γ_{Cha}	interface between air channel and solid walls
Γ_{Chf}	interface between fuel channel and solid walls
λ	heat conductivity, W m^{-1} K^{-1}
Φ	electrical potential, V
ρ	electrical resistivity, W^{-1} m K
σ	electrical conductivity, W m^{-1} K^{-1}
Ω_S	solid part of the physical domain

Subscripts

a	air
f	fuel
i	chemical species
R	reforming reaction
S	shift reaction

Acknowledgements

This work was supported by Gaz de France and ADEME (Agence de l'Environnement et de la Maîtrise de l'Energie).

References

[1] A.J. Appleby and F.R. Foulkes, *Fuel Cell Handbook*, Van Nostrand Reinhold, New York, 1989.

[2] J.R. Selman, How to model solid oxide fuel cells, *Proc. IEA Workshop, Charmey, Switzerland, 1989.*

[3] J.R. Ferguson, Analysis of temperature and current distributions in planar SOFC designs, *2nd Int. Symp. Solid Oxide Fuel Cells, Athens, Greece, 2–5 July 1991.*

[4] J.R. Ferguson, J.M. Fiard and R. Herbin, A two-dimensional simulation of a solid oxide fuel cell, *IEA Workshop: Fundamental Barriers to SOFC performance, Lausanne, Switzerland, Aug. 1992*, OFEN, Berne, Switzerland.

[5] J.M. Fiard and R. Herbin, Numerical simulation of solid oxide fuel cells at the cell and stack level, *Eurogas 92, Trondheim, Norway, June 1992*, NTH-SINTEF, Norway.

[6] F.G. Debenedetti and C.G. Vayenas, *Chem. Eng. Sci., 38* (1983) 1817–1823.

[7] E. Achenbach, Three dimensional and time-dependent simulation of a planar solide oxide fuel cell stack, *J. Power Sources, 49* (1994) 338–348.

[8] Ch. Rechenauer, Dreidimensionale mathematische Modellierung des stationären und instationären Verhaltens oxidkeramischer Hochtemperatur-Brennstoffzellen, *Ph.D. Thesis*, KFA-Jülich, Germany, 1993.

[9] E. Achenbach with KFA-IER, Status of the IEA-bench mark test 1 on stack-modelling, *IEA Workshop, Rome, Italy, 22–23 Apr. 1994.*

[10] K. Nisancioglu and H. Karoliussen, Cell and stack optimisation by modelling, *Proc. 1st Eur. Solid Oxide Fuel Cells Forum, Lucerne, Switzerland, October 1994.*

[11] R. Ødegård, H. Karoliussen and K. Nisancioglu, Comparison of experimental results and a mathematical model for simulation of SOFC stack performance, *6th IEA Workshop and Experts Meet. Advanced Solid Oxide Fuel Cells, Rome, Italy, 1994.*

[12] S.V. Patankar, Numerical heat transfer and fluid flow, Minkowycz and Sparrow (eds.), *Series in Computational Methods in Mechanics and Thermal Sciences*, McGraw-Hill, New York, 1980.

[13] R. Eymard, T. Gallouët and R. Herbin, The finite volume method, in Ph. Ciarlet and J.L. Lions (eds.), *Handbook of Numerical Analysis*, North-Holland.

[14] A. Malandrino and M. Chindemi, Effect of cell configuration and fuel on SOFC modelling, in Singhal et Iwahara (eds.), *Proc. 3rd Int. Symp. Solid Oxide Fuel Cells, Honolulu, HI, USA, May 1993*, pp. 16–21.

[15] J.M. Fiard and R. Herbin, Comparison between finite volume and finite element methods for an elliptic system arising in chemistry, *Comput. Methods Appl. Mech. Eng., 115* (1994) 315–338.

[16] R.B. Bird, W.E. Steward and E.N. Lightfoot, *Transport Phenomena*, Wiley, New York, 1960.

[17] A.L. Lee, Internal reforming development for solid oxide fuel cells, *DOE/MC/22045-2364, Rep. Institute of Gas Technology, 1987.*

[18] M. Bernier and R. Herbin, Numerical solution to a heat transfer problem with radiation boundary conditions, in preparation.

[19] M. Bernier, Maintenance et développement d'un simulateur de pile au gaz naturel, *Université de Savoie, France, 1994.*

[20] H. Karoliussen, K. Nisancioglu and R. Ødegård, The role of certain design and operating parameters on SOFC stack performance, *6th IEA Workshop and Experts Meet. Advanced Solid Oxide Fuel Cells, Rome, Italy, 1994.*

[21] U.G. Bossel and J.R. Ferguson, Natural gas fuelled solid oxide fuel cells and systems, facts and figures, *IEA Workshop, Charmey, Switzerland, 1989.*

[22] H. Karoliussen, K. Nisancioglu, A. Solheim and R. Ødegård, SOFC stack modelling with reforming, *Proc. 3rd Int. Symp. Solid Oxide Fuel Cells, Honolulu, HI, USA*, The Electrochemical Society, Pennington, NJ, USA, 1993.

[23] Draper, Solid oxide fuel cell generator, *US Patent No.* (Apr. 1994).

[24] C.A. Forges and J.F. Pierre, The solid fuel cell future, *IEEE Spectrum,* (Oct.) (1993) 40–44.

[25] J. Hartvigsen, S. Elangovan and A. Khandkar, Modeling design and performance of solid oxide fuel cells, S.P.S. Badwal, M.J. Bannister and R.H.J. Hannink (eds.), *Science and Technology of Zirconia V,* Technomic, 1993.